Atmospheric Plasma Meets Cell: Plasma Tailoring by Living Cells
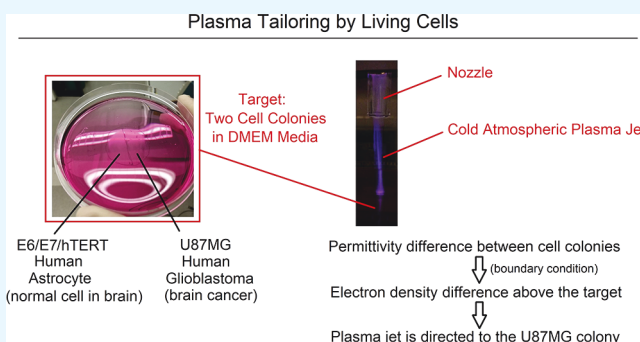
Li Lin,* Dayun Yan, Eda Gjika, Jonathan H. Sherman, and Michael Keidar

Department of Mechanical and Aerospace Engineering, The George Washington University, 800 22nd Street NW, Washington, D.C. 20052, United States of America

S *Supporting Information*

ABSTRACT: The applications of the cold atmospheric plasma jet (CAPJ) in cancer treatment have been investigated for over a decade, focused on the effect that the CAPJ creates on cancer cells. Here we report for the first time on the impact that cells have on the CAPJ during treatment. To better understand these CAPJ−cell interactions, we analyzed the CAPJ behaviors in the presence of several normal and cancer cell lines and investigated the CAPJ selectivity. A more in-depth study of plasma self-organization patterns utilizing a model which contains a combination of normal and cancer cells reveals that the cells' capacitance can be an important predictor of plasma jet behavior. Cancer cells can direct the jet

Plasma Tailoring by Living Cells

either toward or away from normal cells, which depends on the boundary condition behind the cell colony. Both experimental and theoretical results show that a grounded copper board beneath the cell-culture dish leads to opposite CPAJ behaviors compared with a floating boundary condition. In conclusion, our findings indicate that plasma can be self-adaptive toward cancer cells, and such a feature can be manipulated. Therefore, using the permittivity difference among cell lines may help us focus plasmas upon cancer cells at the vicinity of normal tissues and maximize the selectivity of plasma treatments.

KEYWORDS: plasma medicine, selective treatment, cold atmospheric plasma, cell feedback, self-organization pattern, capacitance imaging

INTRODUCTION

The cold atmospheric plasma (CAP) has wide applications in modern medicine, material processing, environmental engineering, and agriculture.[1−4] One of the most significant applications of the cold atmospheric plasma jet (CAPJ) is the selective treatment which causes cell death in cancer cells while having a limited effect on normal cells.[5] In a previous study, we reported that human neuroblastoma cells show a more significant reduction in cell viability compared to healthy fibroblasts when undergoing the same CAPJ treatment conditions.[6] Similarly, after CAPJ treatment, a more significant percentage of adherent lung cancer cells detached from the cell culture plate, while the bronchial epithelial cells continue to remain attached to the substrate.[7] This specific anticancer effect is related to the tumor suppressor gene p53.[8] In a recent study, we compared ten cancer cell lines and revealed that the anticancer capacity of the CAPJ treatment was inversely proportional to the extracellular H_2O_2 consumption rate.[9]

However, for a better understanding of the interaction between the CAPJ and its biomedical targets, it is essential to understand how the CAPJ operates. A typical CAPJ is generated by feeding a noble gas through a pair of electrodes with couple kV sinusoidal waves or pulses at radio frequency.[10] When the discharge voltage is approaching its peak, the free electrons naturally existing in the gas are driven toward the anode.[11] During their travels, some of these electrons collide with other neutral atoms and molecules. For those electrons

with enough kinetic energy, electron-impact ionizations occur during the collisions and provide more electrons to ionize more particles. This process is referred to as "avalanche".[11] During the avalanche, not all electrons can ionize, but more electrons have lower energy and can excite other species. This makes the avalanche region luminous, which is thus referred to as the "plasma bullet" for its bullet-like appearance.[12] On the other hand, during the avalanche, the newly generated electrons are accelerated to the anode, while other species such as positive ions remain almost stationary since they are much heavier than electrons.[11] Therefore, a positive ion cloud appears and turns into a new anode, which attracts the free electrons at the front to start another avalanche.[11] The ion cloud is also known as the "streamer head" and leaves a quasi-neutral plasma column behind, connecting the streamer head and the anode.[11] This is how the plasma bullet propagates forward. Such a process is also referred to as the "ionization wave" because it is an ionization process (plasma bullet) propagating forward.[13] The entire process usually repeats in the same frequency as the discharge voltage waveform. Therefore, the "plasma bullet" cannot be observed by the naked eye but only through a high-speed camera, and the entire CAPJ appears as a continuous luminous beam for the
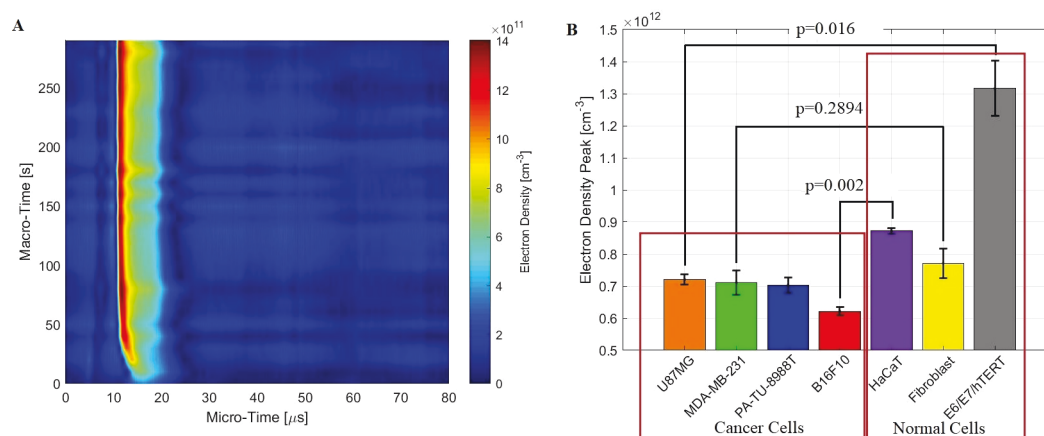
Figure 1. Resulting electron densities in the plasma jet during treatments. (A) An example of spatially averaged and temporally resolved electron density of the CAPJ during the treatment of E6/E7/hTERT cells. (B) A summary of all electron density peaks of the plasma jet at a steady state for different cell lines. Error bars indicate the standard deviations of measurement repeats.

naked eye. In addition, during the propagation, hundreds of plasma chemistry reactions generate reactive nitrogen species (RNS) and reactive oxygen species (ROS) along with the electromagnetic wave emission (from radio frequency to ultraviolet) as a result of particle collisions during the ionization wave propagation in ambient air.[14,15]

During the propagation process of the CAPJ, the gas flow rate, the discharge voltage, waveform, frequency, and power are some of the critical parameters that control the CAPJ. These parameters can influence the chemical composition, its corresponding optical emission spectrum (OES),[16−18] and the behavior of the plasma bullet.[19,20] The CAPJ is also affected by the environmental humidity, the impurity of the noble gas supply, and the feeding gas type, which can also be used to manipulate the electron temperature and chemical compositions of the CAPJ.[21−23]

Another set of critical parameters are based on the properties of the target which is a boundary condition of CAPJs. The thickness of a dielectric target below the jet can affect the plasma bullet behavior and the species flux.[24] Also, the distance from the target can influence the chemical composition of the CAPJ.[25] However, all previous biomedical studies of CAPJs focus on the treatment without taking into account the target feedback effect on the CAPJ. During any CAPJ treatments, targets (i.e., cancer cells) can also alter the plasma as a boundary condition of both electromagnetism and plasma chemistry such as the release and deposition of species.[26] In other words, two CAPJs with identical hardware settings are different when treating different types of cells.

In this work, we discover the effect of living cells on the CAPJ by analyzing its spatially averaged electron density, the capacitance distribution of the target, and the temporally averaged brightness distribution at the CAPJ−target contact surface, which is also known as self-organization pattern (SOP).[27,28] Free electrons in the CAPJ are the origin of ionizations and attachments which produce positive and negative ions. Electrons determine the electric field strength of the streamer head, and they are also involved in the generation of all reactive species, either directly or indirectly.[29] Electron density is also a critical parameter for estimating other properties of the CAPJ, such as electron temperature.[19,30] The SOP indicates how the ionization wavefront distributes at the vicinity of the target since the electrons which ionize species

during collisions contribute to the high-energy tail of the electron energy distribution function (EEDF), while at the same location, more electrons can merely excite chemical species and provide the OES.[30] Capacitance imaging implies how electron density and SOP are related to the target permittivity. These results and conclusions from the *in vitro* experiments are then supported by a theoretical analysis which also suggests how other CAPJs and target parameters can be used to manipulate their interactions. Based on the findings of a cell feedback signal in this work, future research studying self-adaptive plasma will assess the ability of the CAPJ to optimize itself and consequently fit a variety of applications.[31−34]

■ RESULTS

Electron Density. We first investigated how the electron density of the CAPJ is altered by cells immersed in the medium, which is named as "cell-medium target" in this work. Figure 1A illustrates an example of the temporally resolved electron density captured by the Rayleigh microwave scattering (RMS) system when the CAPJ is treating E6/E7/hTERT cells. The contour plot was depicted in a 2D time domain where the color bar represents the value of electron density. The horizontal "microtime" axis represents the time in a discharge period, while the vertical "macrotime" axis represents the time after the power was switched on. For each discharge period, an electron density peak appeared at about 10 μs of the microtime. From 0 to 50 s of the macrotime, a lower electron density peak with later appearance indicated a warm-up time before the plasma jet reached its steady state. In such a steady state (from about 50 to 300 s of the macrotime), the electron density peaks had constant height and appearance time with limited disturbance. All electron densities discussed below in this paper refer to the peak values at steady states of the working CAPJ.

Figure 1B summarizes the measured electron density peaks of CAPJs with different cell lines as targets. Among the different cell lines tested, cancer cells resulted in an overall lower electron density than normal cells. For instance, the electron densities of U87MG and B16F10 cancer cells were significantly lower than those of the healthy E6/E7/hTERT and HaCaT cells. An exception was the MDA-MB-231 breast cancer cells and the healthy primary fibroblast. The difference in electron density was not statistically significant for these two
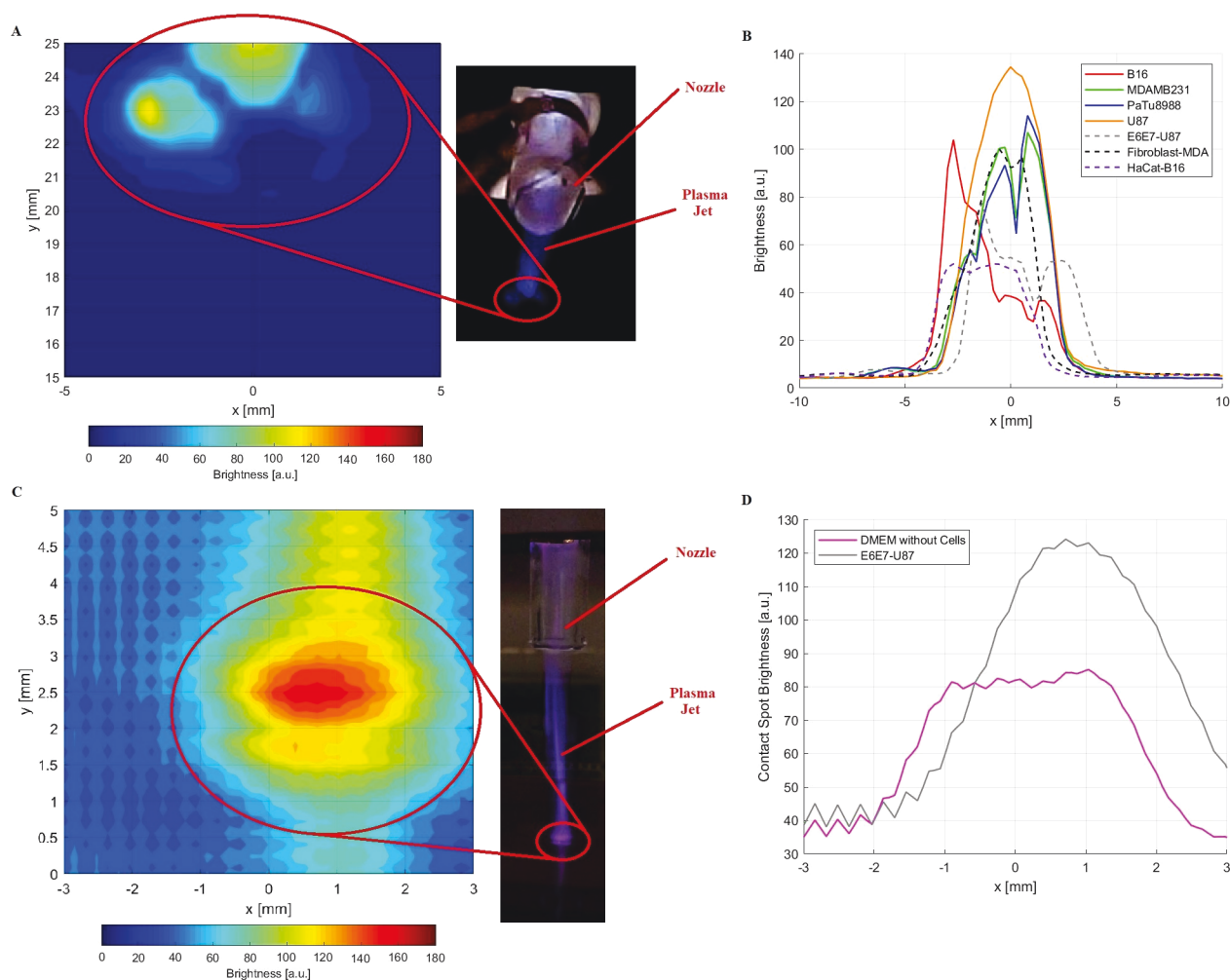
Figure 2. Self-organization patterns when the plasma jet is directed to the boundary of cell colonies. (A) A bottom-view example of the no-cell region at the negative-x region and B16F10 at the positive-x region. (B) The brightness summary of the bottom-view self-organization patterns that taking average brightness from $y = 22.5$ mm to 23.5 mm for each case. (C) A side-view example of E6/E7/hTERT at the negative-x region and U87MG at the positive-x region with a grounded copper plate beneath the dish. (D) The brightness summary of the side-view self-organization patterns that take average brightness from $y = 1.5$ mm to 3.5 mm.

cell lines even though breast cancer cells had a lower average electron density. These results suggest that cancer cells, as a target, may weaken the plasma jet.

Self-Organization Pattern. The SOP is a luminous CAPJ−target contact region. According to the mechanism of streamer propagation, the luminous region is where the "avalanche" occurs. Therefore, the brightness distribution of the SOP indicates where the CAPJ propagates. Our study relies on single and double cell experimental setups for investigating plasma self-organization patterns. For each single-cell test, the cell colony was located at the positive-x region on the right, while the no-cell region locates at the negative-x region. The CAPJ was aligned to shoot at the boundary of the colony ($x = 0$ mm). For each double-cell test, the normal cell colony was located at the negative side, and the cancer cell colony was located at the positive side with their boundary located at $x = 0$ mm for the CAPJ to aim at. An example of the single B16F10 test is shown in Figure 2A. There was an obvious bright dot at around $x = -3$ mm and $y = 23$ mm, while there was no such brightness at the positive x side. Note that the brightness at the top of this image was from the plasma jet rather than the SOP. Therefore, the SOP of the CAPJ shooting at the boundary of

the B16F10 colony was asymmetric. To strictly quantify the symmetry, the brightness value summations between $y = 22.5$ and 23.5 mm for all cases were summarized in Figure 2B. It is clear that B16F10 "pushes" the brightness away to the no-cell region at the negative-x side, while the other three cancer cells lines have no such significant asymmetry. Recall that in Figure 1B B16F10 made the lowest electron density, while the other cancer cells lines result in significantly higher electron densities in the CAPJ. Moreover, Figure 2B also shows the SOP of the double-cell test. When B16F10 was seeded on the right of HaCaT, more brightness had been observed on the HaCaT side. Similarly, when U87MG was seeded on the right of E6/E7/hTERT, more brightness was observed on the E6/E7/hTERT side. However, such an effect was not strong when MDA-MB-231 was on the right of the fibroblast. Also recall that in Figure 1B the difference of "B16F10 versus HaCaT" and "U87MG versus E6/E7/hTERT" was significant, while the difference of "MDA-MB-231 versus fibroblast" was not significant. These trends imply that the cell line which makes a lower electron density in CAPJ can "push" the SOP away. Actually, the SOP results can be easily explained based on the electron densities shown in Figure 1B. The cell colony which
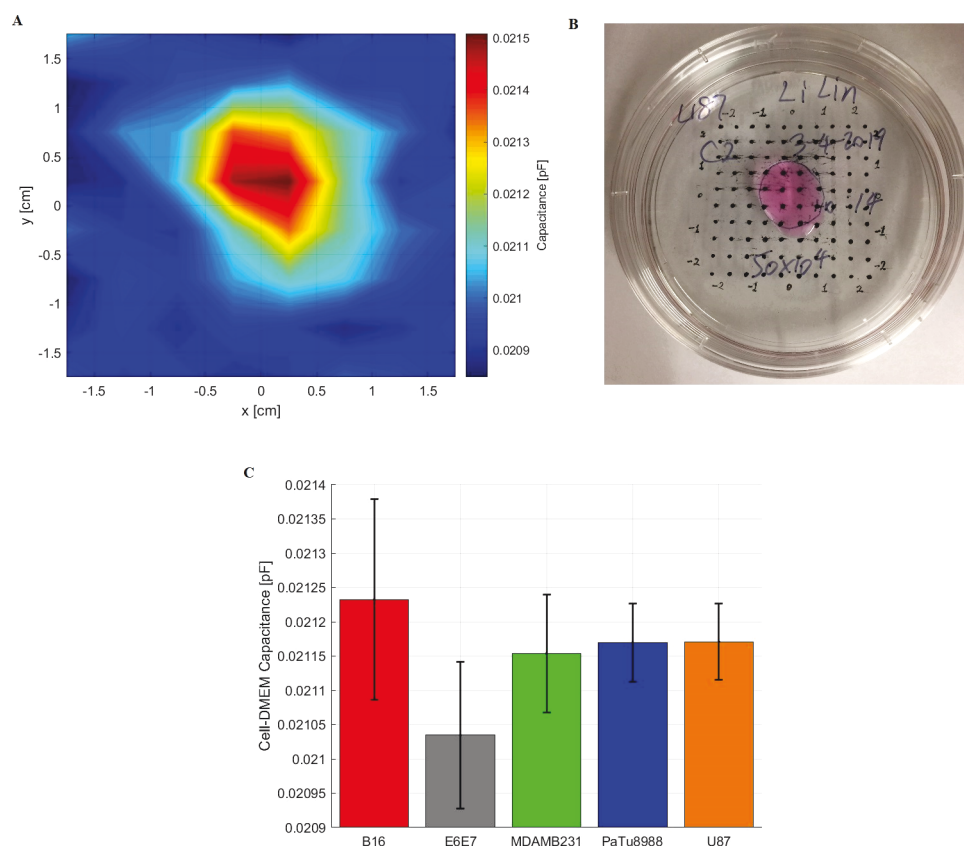
Figure 3. Capacitance imaging of the cell colonies at the centers of dishes. (A) An example of capacitance imaging of U87MG. (B) The photo of a 500 μL U87MG cell solution. (C) The comparison of average capacitance in the square region of x and y from −1.00 to 1.00 cm. Error bars represent the standard deviations of the cell colony capacitance.

could result in a lower electron density was supposed to result in less excited species. In the case of the cancer cell colony on the right of the normal cell one, more free electrons which are involved in the "avalanche" above the normal cell colony could make the streamer propagate to the normal cell side and thus appeared as an asymmetric SOP. Therefore, the electron density is reflecting how cancer cells propel the CAPJ toward normal cells in the double-cell cases. Namely, the cell colonies direct the CAPJ in selecting where or which target to treat.

However, such a phenomenon can be reversed when placing a ground electrode under the cell culture dish. Due to the blockage of the copper plate from the bottom and the CAPJ generator from the top, only the side view was provided for this extra experiment. Figure 2C shows a side-view example of the CAPJ directed at the boundary between E6/E7/hTERT and U87MG colonies covered by 20 mL of DMEM medium. The contact spot appeared as a bright ellipse. Figure 2D shows the comparison between "E6/E7/hTERT versus U87MG" and pure DMEM, which were the average brightness taken from y = 1.5 mm to 3.5 mm. For comparison, the contacted spot brightness distribution for the pure DMEM case was symmetric. In contrast, the contacted spot was inclined to the right (positive x side) where the U87MG colony was seeded, while the E6/E7/hTERT colony was located at the negative x side. The boundary of these two cell colonies was located at $x = 0$ mm. This result was opposite to the case without an electrode under the dish (Figure 2B). Consequently, we displayed that the target-triggered permittivity effect can be reversed by grounding the cathode. A similar conclusion can be found in another simulation study which

shows that the electric field of streamer propagation is proportional to the target permittivity with a grounded cathode behind.[35] This result might also explain the stronger killing effect of U87MG when compared with E6/E7/hTERT with a metal plate beneath the dish, which had been reported earlier.[36,37]

Capacitance Imaging. During *in vitro* treatments, the cell colonies with media were the targets and also the boundary conditions of the CAPJ. For dielectric targets, it has been previously reported how their permittivity changes the plasma jet.[35] To study the interactions of the electron density, SOP, and such boundary conditions, the permittivity of cell-medium targets was analyzed. Figure 3A shows an example of the imaging where a 500 μL U87MG cell solution was located at the center of the dish, while Figure 3B shows the corresponding photo. This example indicates that a U87MG cell colony has a higher capacitance compared with the surrounding area of the dish. Figure 3C summarizes the average capacitances of five different cell colonies. Data were the average values taken in a square area from −1.0 to 1.0 cm cm for both x and y axes. The average capacitance of the B16F10 colony was the highest, which corresponded to the lowest electron density observed in the plasma jet (Figure 1B). In contrast, the capacitance of the E6/E7/hTERT colony was the lowest, which corresponded to the highest electron density observed in the plasma jet. Since all imaging was performed using the same electrodes (same geometry), the highest capacitance of the B16F10 colony indicated the highest permittivity of B16F10 cells. Similarly, the E6/E7/hTERT colony displayed the lowest capacitance and permittivity. In

short, we conclude that a higher permittivity of the cell colony can make a lower electron density in the CAPJ. The permittivity of cells thus determined where the CAPJ should come into contact with the target. This result might explain the strong resistance to CAPJ treatments of the B16F10 colony compared with all other cancer cell lines as reported in a previous study.[38]

■ DISCUSSION

To understand how the target permittivity could affect the plasma jet with and without a ground electrode, we derived a general mathematical model between the permittivity of the dielectric target and the electric field of the plasma bullet which is a space charge consisting of the streamer head and the target surface charge. The scenario is an electrostatic problem of the moment when the plasma bullet is approaching the vicinity of the target surface. Considering a 1D model, the anode of the CAPJ device locates at 0 cm; a positive ion cloud as the streamer head locates at L_P; the target front surface locates at $L_P + L_B$; and the target thickness is L_T. Therefore, the back surface of the target locates at $L_P + L_B + L_T$. Between the anode and the streamer head, we defined an effective permittivity of the plasma column as

$$\varepsilon_P = \frac{\sigma L_P}{2\pi f A \varepsilon_0}$$

where σ is the conductivity of the plasma column; f is the discharge frequency; A is the cross-section area of the plasma column; and ε_0 is the permittivity of the vacuum. The plasma column conductivity in this model is based on the impedance of a capacitor: $Z = \sigma^{-1} = (2\pi f C)^{-1}$, where C is the capacitance that $C = \varepsilon_0 \varepsilon_P A / L_P$, where ε_P is the effective relative permittivity of the plasma. Since $\sigma = n_{eP} e \mu_e L_P$ and $\mu_e = \frac{e}{m_e \nu_{coll}}$, we have

$$\varepsilon_P = \frac{L_P^2 n_{eP} e^2}{2\pi f A \varepsilon_0 m_e \nu_{coll}} \tag{1}$$

where n_{eP} is the electron density in the plasma column; e is the unit charge; μ_e is the mobility of electron; m_e is the mass of an electron; and ν_{coll} is the electron-neutral collision frequency. The permittivity between the streamer head and target surface is ε_0 since it is a region not yet ionized, and the permittivity of the helium−air mixture is close to the one of vacuum.[39,40] The target permittivity is denoted as ε_T.

The electric field of the plasma bullet defined as the field located at the center point between the streamer head and target surface can be expressed as the superposition of the background electric field (from the electrodes) and the field of charges

$$E_B = E_{B-bg} + \frac{q}{2\pi\varepsilon_0 (L_B/2)^2} \tag{2}$$

where the first term on the right-hand-side E_{B-bg} is the electric field of the electrodes at the bullet position, while the second term is the Coulomb's law of the streamer head and target surface charge. They share the same charge amount of $q = n_B e$ to ensure the charge balance of the entire model, where n_B is the ion density of the streamer head. To evaluate E_{B-bg}, we consider the model of capacitors in series with the equivalent capacitance

$$C_{eq} = \left(\frac{1}{C_P} + \frac{1}{C_B} + \frac{1}{C_T} \right)^{-1} \tag{3}$$

where $C_P = \frac{A\varepsilon_0\varepsilon_P}{L_P}$ is the effective capacitance of the plasma column; $C_B = \frac{A\varepsilon_0}{L_B}$ is the capacitance of the plasma bullet region between the streamer head and target surface; and $C_T = \frac{A\varepsilon_0\varepsilon_T}{L_T}$ is the capacitance of the target. Based on the "voltage divider rule", we have

$$E_{B-bg} = \frac{\varphi_{FS} - \varphi_{SH}}{L_B} = \frac{(\varphi_0 - \varphi_{BS})C_{eq}}{L_B C_B} \tag{4}$$

where φ_{FS}, φ_{SH}, φ_0, and φ_{BS} are the potential at the target front surface, streamer head, anode, and target back surface, respectively. Therefore, eq 2 yields

$$E_B = (\varphi_0 - \varphi_{BS}) / \left(\frac{L_T}{\varepsilon_T} + \frac{L_P}{\varepsilon_P} + L_B \right) + \frac{n_B e}{2\pi\varepsilon_0 (L_B/2)^2} \tag{5}$$

Combining with eq 1, we obtain a general mathematical expression of the plasma bullet electric field

$$E_B = (\varphi_0 - \varphi_{BS}) / \left(\frac{L_T}{\varepsilon_T} + \frac{2\pi f A \varepsilon_0 m_e \nu_{coll}}{L_P n_{eP} e^2} + L_B \right)$$
$$+ \frac{n_B e}{2\pi\varepsilon_0 (L_B/2)^2} \tag{6}$$

When the target back surface is a ground electrode, $\varphi_{BS} = 0$. However, when the target back surface is floating, the potential is determined by the plasma bullet charge which can be considered as a dipole. Thus, the target back surface potential locates at the negative charge side of the dipole and can be calculated as

$$\varphi_{BS} = \Delta\varphi - \frac{n_B e L_B}{4\pi\varepsilon_0 \varepsilon_T (L_B/2 + L_T)^2} \tag{7}$$

where $\Delta\varphi$ is the potential drop along the plasma column which is proportional to n_{eP}^{-1}. Therefore, eqs 6 and 7 explain the entire mechanism behind the phenomena introduced in this work. When the target back surface is attached to a ground electrode, the plasma bullet electric field is proportional to the target permittivity which agrees with the phenomenon shown in Figures 1 and 3, assuming that a higher electric field creates a higher electron density in the CAPJ. When the target back surface is floating, the target permittivity appears in both the numerator and the denominator of the first term in eq 6. Therefore, only when the electron density in the plasma column is low, the bullet electric field is inversely proportional to the target permittivity. This is because the plasma column term $\frac{2\pi f A \varepsilon_0 m_e \nu_{coll}}{L_P n_{eP} e^2}$ dominates and limits the contribution of $\frac{L_T}{\varepsilon_T}$, while $\Delta\varphi$ cannot limit the term $\frac{n_B e L_B}{4\pi\varepsilon_0 \varepsilon_T (L_B/2 + L_T)^2}$ in the numerator since the potential drop in the numerator can at most cancel out the φ_0. In this work, as shown in Figure 1B, the electron density is mostly less than 10^{12} cm^{-3} with 8 kV discharge voltage which is under the "low electron density" situation, considering the same CAPJ generator can achieve an electron density higher than 2×10^{12} cm^{-3} with 5 kV and the same gas flow rate when there is no target.[30] Moreover, eq 6
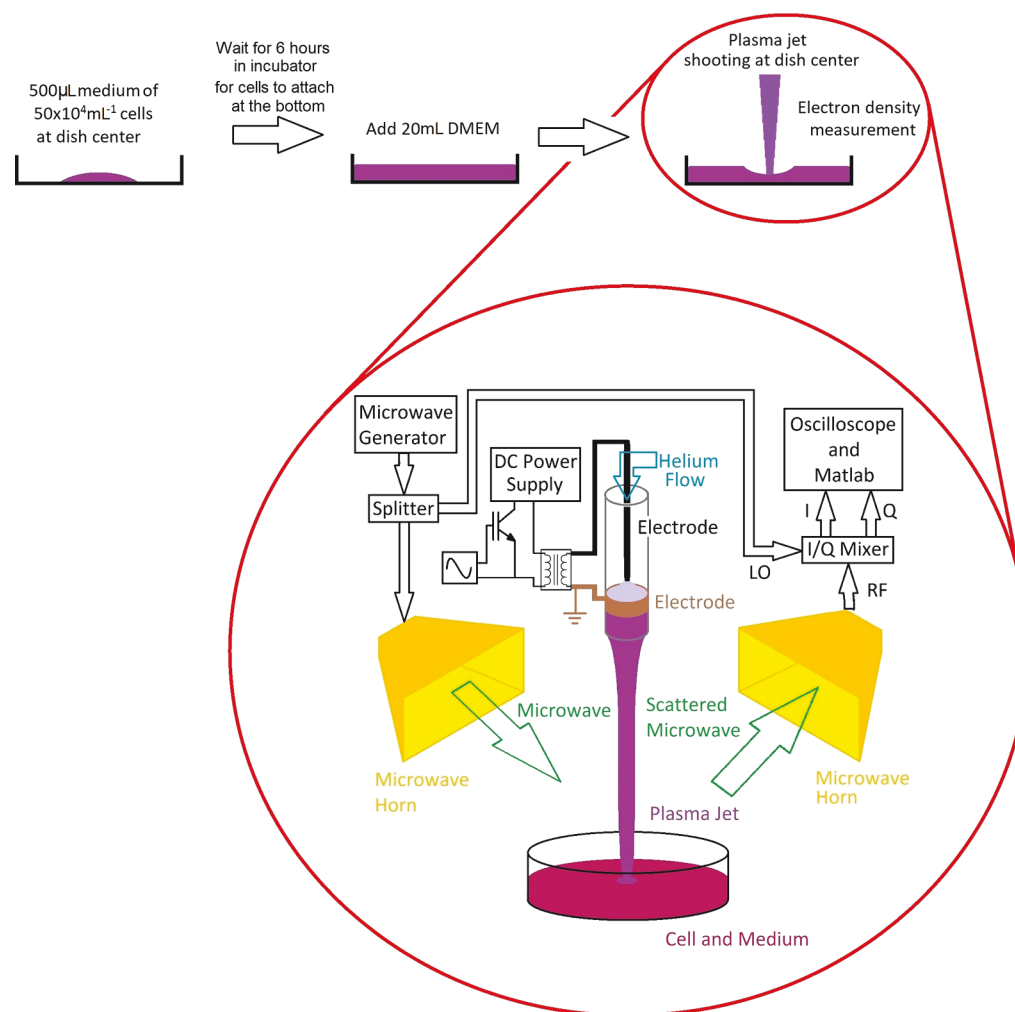
Figure 4. Schematic representation of the *in vitro* experimental setup and a cold atmospheric plasma jet with Rayleigh microwave scattering for performing electron density measurements.

suggests that a lower L_B can increase the term $\frac{n_B e L_B}{4\pi\varepsilon_0\varepsilon_T(L_B/2+L_T)^2}$ and add more limit to the contribution of $\frac{L_T}{\varepsilon_T}$ in the denominator. This agrees with the common sense that the target can affect the plasma bullet more when the streamer is closer to the target. Equations 6 and 7 also indicate additional CAPJ features which agree with other publications. For example, the electric field of a plasma bullet is usually stronger when the ground electrode appears.[41] This is because the φ_{BS} in eq 7 is positive and implies that the potential drop along the plasma column is greater than the potential difference made by the streamer head electric field. In other words: $\varphi_0 - 0 > \varphi_0 - \varphi_{BS}$. However, if the electron density in the plasma column is high enough and results in a low $\Delta\varphi$, the electric field of the streamer head dominates. This explains why the streamer head potential can increase along the plasma jet when the discharge voltage is high, as reported in an old publication.[42] In addition, using the same mathematical model, the electric field inside the target can be easily derived to

$$E_T(z) = (\varphi_0 - \varphi_{BS})/\left(L_T + \frac{\varepsilon_T}{\varepsilon_P}L_P + \varepsilon_T L_B\right) - \frac{n_B e}{4\pi\varepsilon_0\varepsilon_T z^2}$$

(8)

where z is the location in the target from the target front surface. The right-hand side is inversely proportional to the target permittivity. However, the first term is positive, and the second one is negative. This equation suggests that the electric field in the target can be inversely proportional to the target permittivity, which agrees with the simulation results published previously.[35] However, due to the negative second term, this equation also indicates that such a feature occurs only when the electric field of the streamer does not dominate. Please note that eq 8 is less relevant to the main topic of this work, but more discussion of it can be found in the Supporting Information.

Other features of the CAPJ implied by this mathematical model include the decay of the plasma bullet electric field along the propagation distance, the weakening of the target inner electric field for a further target position, and the strengthening of it when the streamer head is closer to the target. These trends all agree with common sense. Overall, these equations can be utilized to manipulate the CAPJ, and they will be used in the future for optimization and self-adaptive control. As an additional example, a finite element simulation of an electrostatic model using the software FEMM is discussed in the Supporting Information.

In this study, we revealed how the permittivity of the cell colony could alter the direction of the CAPJ during the *in vitro*
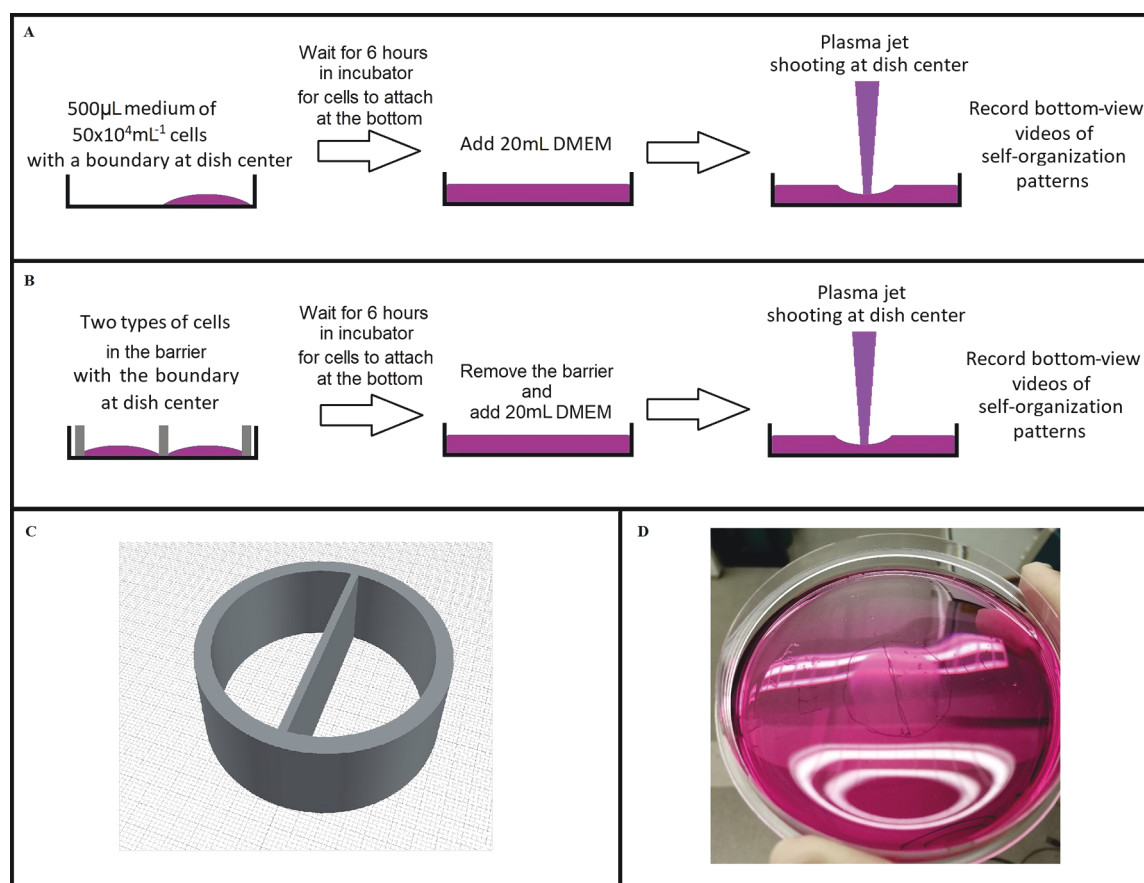
Figure 5. *In vitro* cell culture for observing the self-organization patterns of CAPJ. (A) The cell preparation procedure of one cell line. (B) The procedure of the double-cell test. (C) The 3D model of the cell barrier. (D) The E6/E7/hTERT cell colony (left) and U87MG cell colony (right) in 20 mL of DMEM medium.

treatment. We conclude that the electron density of the CAPJ can be affected by the permittivity of the targeted cell colony. When there is no electrode beneath the cells, a higher permittivity of the cell colony could result in a lower electron density for the plasma jet. This causes the plasma jet to lean more on one side by being directed at the boundary between two cell lines or the boundary of a single-cell colony. When a ground electrode is placed under the cell colony, such a targeted permittivity effect can be reversed. Therefore, when there are two or even more cell lines facing the plasma jet, the cell permittivity can affect the CAPJ by determining which target the CAPJ will come into contact with. Based on the mathematical relationship we derived and supplemented with the FEMM simulation, we also revealed the mechanism of such a targeted permittivity effect. This study provides a strong basis for a further understanding of selective cancer treatment, adaptive plasma control, and future possible clinical applications.

■ MATERIALS AND METHODS

Cell Culture. Four cancer cell lines were investigated in this study, including B16F10 (murine melanoma), MDA-MB-231 (human breast adenocarcinoma), PA-TU-8988T (human pancreatic adenocarcinoma), and U87MG (human glioblastoma). In addition, three normal cell lines were also investigated, including E6/E7/hTERT (human astrocyte), HaCaT (human keratinocytes), and mouse primary fibroblasts. The U87MG cells were purchased from the American Type Culture Collection (ATCC), while the rest of the cell lines were donated from other laboratories at the George Washington

University. Cell lines U87MG, MDA-MB-231, PA-TU-8988T, E6/E7/hTERT, and the primary mouse fibroblasts were cultured in DMEM medium (Life Technologies, 11965−118) supplemented with 10% (v/v) fetal bovine serum (Atlanta Biologicals, S11150) and 1% (v/v) penicillin/streptomycin. The B16F10 cells were cultured in RPMI-1640 (ATCC, 30-2001) also supplemented with 10% (v/v) fetal bovine serum and 1% (v/v) penicillin/streptomycin, and the HaCaT cells were cultured in Keratinocyte-SFM medium (Gibco) with supplements (Gibco; 37000-15) and 0.5% (v/v) penicillin/streptomycin. Cells were seeded at a concentration of 5×10^5 cell/mL, and the cell cultures were maintained under standard conditions at 37 °C in a humidified incubator containing 5% CO_2.

Electron Density Measurement. As shown in Figure 4, 500 μL cells in medium (5×10^5 cell/mL) were carefully seeded at the center of a 100 mm cell culture dish for each cell line. Cells were cultured for 6 h under standard cell culture conditions. During this period, the cells were able to attach to the dish, which is critical for establishing *in vitro* cell growth. After the incubation was complete, 20 mL of DMEM medium was added before proceeding with measurements.

A schematic of the CAPJ generator is illustrated in Figure 4 along with the hardware for measuring the electron density of the plasma jet: the Rayleigh Microwave Scattering (RMS) system. The CAPJ in this work was generated by a 10 LPM helium flow passing through a pair of electrodes powered by an 8 kV pk−pk sinusoidal wave at 12.5 kHz. In this experiment, the propagation of the CAPJ was a cathode-directed streamer. Therefore, the streamer head was positively charged. For the temporally resolved electron density measurement, the cell-medium target was 3 cm away from the nozzle. A microwave of 12.6 GHz was generated and emitted from a horn antenna. The microwave beam was then scattered by the plasma jet which was considered as a dipole.[43] The scattered wave carried the information
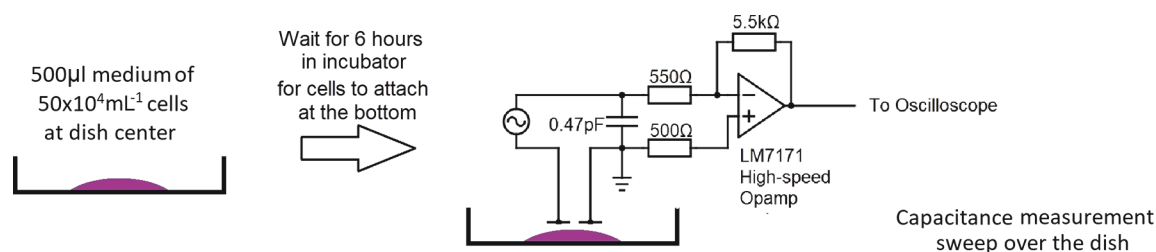
Figure 6. Schematic illustration of the capacitance imaging.

on conductivity as a function of electron density which was recorded by Matlab in real time through an oscilloscope. More details of the RMS diagnostic technology can be found in an old publication.[43]

Observation of the Plasma Self-Organization Pattern. The experiment of the SOP includes two different setups: the single-cell setup and the double-cell setup. The procedure of the single-cell setup is shown in Figure 5A. As part of this setup, 500 μL of cells in the medium was carefully seeded at a 1 cm distance from the center of the 100 mm cell culture dish. In this manner, the boundary of each cell population aligned with the axis of the plasma jet. In other words, the plasma jet was applied at the boundary of the cell colony. Similarly, cells were incubated for 6 h under standard experimental conditions. After the incubation was complete, 20 mL of medium was added, and the SOP for each cell line was recorded. The protocols of the double-cell test procedure are shown in Figure 5B. For this setup, we designed a plastic cell barrier to separate the two cell colonies during the incubation as shown in Figure 5C. The barrier was positioned at the center of the 100 mm cell culture dish. One normal cell line and another cancer cell line were seeded in the two wells of the barrier. In each well, 500 μL of cells in medium (5×10^5 cells/mL) was added. Cells were incubated for 6 h. After the incubation, the barrier was removed, creating a small gap between the two cell colonies as shown in Figure 5D. This gap represents the boundary between the two cell colonies. To quantify the SOP, a camera was fixed below the dish, and we recorded a bottom view of the SOP video during the CAPJ treatment in each test. Using the Matlab command "VideoReader", each video frame was converted to a matrix of optical brightness distributions. The summation of all the test frames divided by the number of frames thus represented the average brightness distribution of the dynamic SOP video. For each single-cell line test, the center of the cell colony was located 1 cm from the center of the dish. This allowed the CAPJ nozzle to be pointed at the boundary of each colony and to show how the presence of cells can make the SOP asymmetric. In each double-cell experiment, the difference between cell lines was also expected to reflect a certain asymmetry.

Capacitance Imaging. For the capacitance imaging, the cell colony was located at the center of the dish (Figure 6). A sinusoidal wave (10 V pk-pk, 25 MHz) was applied on the series of a 0.47 pF reference capacitor and a pair of copper electrodes (5 mm × 1 cm each with a 1 mm gap). The electrodes were attached to a linear translation stage for position control. The electrodes were 1 mm away from the surface of the medium and swept over the dish during each measurement for the imaging. Once the sample permittivity changed, the impedance between the electrodes changed accordingly along with the voltage applied to the reference capacitor. This voltage signal was sent to a 10× signal multiplier circuit with a core of LM7171 high-speed operational amplifier before it was finally sent to the oscilloscope and recorded in Matlab.

ASSOCIATED CONTENT

Ⓢ Supporting Information

The Supporting Information is available free of charge on the ACS Publications website at DOI: 10.1021/acsami.9b10620.

Figure S1. An electrostatic simulation model of a streamer propagation at the vicinity of a dielectric target. Figure S2. Average electric field of the streamer head space charge. Figure S3. Average electric field in the target. Figure S4. The axial potentials and electric fields of the target back surface with and without grounding the electrode (PDF)

AUTHOR INFORMATION

Corresponding Author
*E-mail: lilin@gwu.edu.

ORCID Ⓘ
Li Lin: 0000-0003-0176-8858
Eda Gjika: 0000-0002-6700-4394

Author Contributions
M.K. provided the initial idea that the cell colony capacitance may play a key role in the CAPJ–cell interactions. L.L. and D.Y. are responsible for the cell culture and preparation of B16F10, E6/E7/hTERT, MDA-MB-231, PA-TU-8988T, and U87MG. E.G. was responsible for the cell culture and preparation of HaCaT and fibroblast. L.L. also contributed to the measurement and data processing of CAPJ electron density, SOP, and capacitance imaging. L.L. developed the 1D mathematical model and simulated the 2D electrostatic scenario in FEMM. All authors are involved in the text editing.

Notes
The authors declare no competing financial interest.
Significance Statement. Cold plasma cancer therapy is currently one of the hottest topics in plasma engineering. The advantage of plasma treatment of cancer is its selectivity that may lead cancer cells to apoptosis with limited damage to normal cells (limited side effects). However, previous research focuses on comparing cell viabilities among different cell lines with the same plasma treatments. In this work, we describe a discovery that cells can affect the plasma. Based on our analysis of such cell feedback effects, future optimization of the plasma treatment can be achieved, and personalized treatment based on plasma adaptation can be envisioned.

REFERENCES

(1) Fridman, A.; Kennedy, L. *Plasma Physics and Engineering*; Taylor & Francis: New York, 2004.
(2) Levchenko, I.; Xu, S.; Teel, G.; Mariotti, D.; Walker, M. L. R.; Keidar, M. Recent Progress and Perspectives of Space Electric

Propulsion Systems Based on Smart Nanomaterials. *Nat. Commun.* **2018**, *9*, 879.

(3) Xie, J.; Chen, Q.; Suresh, P.; Roy, S.; White, J. F.; Mazzeo, A. D. Paper-based Plasma Sanitizers. *Proc. Natl. Acad. Sci. U. S. A.* **2017**, *114*, 5119−5124.

(4) Keidar, M.; Yan, D.; Sherman, J. H. *Cold Plasma Cancer Therapy*; Morgan & Claypool Publishers: San Rafael, CA, 2019.

(5) Yan, D.; Sherman, J. H.; Keidar, M. Cold Atmospheric Plasma, aNovel Promising Anti-cancer Treatment Modality. *Oncotarget* **2017**, *8*, 15977−15995.

(6) Keidar, M.; Shashurin, A.; Volotskova, O.; Stepp, M. A.; Srinivasan, P.; Sandler, A.; Trink, B. Cold Atmospheric Plasma in Cancer Therapy. *Phys. Plasmas* **2013**, *20*, 057101.

(7) Keidar, M.; Walk, R.; Shashurin, A.; Srinivasan, P.; Sandler, A.; Dasgupta, S.; Ravi, R.; Guerrero-Preston, R.; Trink, B. Cold Plasma Selectivity and the Possibility of a Paradigm Shift in Cancer Therapy. *Br. J. Cancer* **2011**, *105*, 1295−1301.

(8) Ma, Y.; Ha, C. S.; Hwang, S. W.; Lee, H. J.; Kim, G. C.; Lee, K.-W.; Song, K. Non-thermal Atmospheric Pressure Plasma Preferentially Induces Apoptosis in p53-mutated Cancer Cells by Activating ROS Stress-response Pathways. *PLoS One* **2014**, *9*, 0091947.

(9) Yan, D.; Lin, L.; Sherman, J. H.; Canady, J.; Trink, B.; Keidar, M. The Correlation Between the Cytotoxicity of Cold Atmospheric Plasma and the Extracellular H_2O_2Scavenging Rate. *IEEE Trans. Radiat. Plasma Med. Sci.* **2018**, *2*, 618−623.

(10) Schutze, A.; Jeong, J. Y.; Babayan, S. E.; Park, J.; Selwyn, G. S.; Hicks, R. F. The Atmospheric-Pressure Plasma Jet: AReview and Comparison to Other Plasma Sources. *IEEE Trans. Plasma Sci.* **1998**, *26*, 1685−1694.

(11) Keidar, M.; Beilis, I. *Plasma Engineering: Applications from Aerospace to Bio and Nanotechnology*; Academic Press, 2013.

(12) Lu, X.; Laroussi, M. Dynamics of an Atmospheric Pressure Plasma Plume Generated by SubmicrosecondVoltage Pulses. *J. Appl. Phys.* **2006**, *100*, 063302.

(13) Lu, X.; Ostrikov, K. K. Guided Ionization Waves: The Physics of Repeatability. *Appl. Phys. Rev.* **2018**, *5*, 031102.

(14) Liu, Z.; Xu, D.; Liu, D.; Cui, Q.; Cai, H.; Li, Q.; Chen, H.; Kong, M. G. Production of Simplex RNS and ROS by Nanosecond Pulse N_2/O_2Plasma Jets with Homogeneous Shielding Gas for Inducing Myeloma Cell Apoptosis. *J. Phys. D: Appl. Phys.* **2017**, *50*, 195204.

(15) Xiong, Q.; Lu, X.; Liu, J.; Xian, Y.; Xiong, Z.; Zou, F.; Zou, C.; Gong, W.; Hu, J.; Chen, K.; Pei, X.; Jiang, Z.; Pan, Y. Temporal and Spatial Resolved Optical Emission Behaviors of a Cold Atmospheric Pressure Plasma Jet. *J. Appl. Phys.* **2009**, *106*, 083302.

(16) Uchida, G.; Takenaka, K.; Kawabata, K.; Setsuhara, Y. Influence of He Gas Flow Rate on Optical Emission Characteristics in Atmospheric Dielectric-Barrier-Discharge Plasma Jet. *IEEE Trans. Plasma Sci.* **2015**, *43*, 737−744.

(17) Pei, X.; Lu, Y.; Wu, S.; Xiong, Q.; Lu, X. A Study on the Temporally and Spatially Resolved OH Radical Distribution of a Room-temperature Atmospheric-pressure Plasma Jet by Laser-induced Fluorescence Imaging. *Plasma Sources Sci. Technol.* **2013**, *22*, 025023.

(18) Jarrige, J.; Laroussi, M.; Karakas, E. Formation and Dynamics of Plasma Bullets in a Non-thermal Plasma Jet: Influence of the High-voltage Parameters on the Plume Characteristics. *Plasma Sources Sci. Technol.* **2010**, *19*, 065005.

(19) Walsh, J. L.; Kong, M. G. Frequency Effects of Plasma Bullets in Atmospheric Glow Discharges. *IEEE Trans. Plasma Sci.* **2008**, *36*, 954−955.

(20) Xiong, Q.; Lu, X.; Xian, Y.; Liu, J.; Zou, C.; Xiong, Z.; Gong, W.; Chen, K.; Pei, X.; Zou, F.; Hu, J.; Jiang, Z.; Pan, Y. Experimental Investigations on the Propagation of the Plasma Jet in the Open Air. *J. Appl. Phys.* **2010**, *107*, 073302.

(21) Lin, L.; Lyu, Y.; Trink, B.; Canady, J.; Keidar, M. Cold Atmospheric Helium Plasma Jet in Humid Air Environment. *J. Appl. Phys.* **2019**, *125*, 153301.

(22) Schmidt-Bleker, A.; Winter, J.; Iseni, S.; Dünnbier, M.; Weltmann, K.-D.; Reuter, S. Reactive Species Output of a Plasma Jet with a Shielding Gas Device - Combination of FTIR Absorption Spectroscopy and Gas Phase Modelling. *J. Phys. D: Appl. Phys.* **2014**, *47*, 145201.

(23) Sarani, A.; Nikiforov, A. Y.; Leys, C. Atmospheric Pressure Plasma Jet in Ar and Ar/H_2O Mixtures: Optical Emission Spectroscopy and Temperature Measurements. *Phys. Plasmas* **2010**, *17*, 063504.

(24) Breden, D.; Raja, L. L. Computational Study of the Interaction of Cold Atmospheric Helium Plasma Jets with Surfaces. *Plasma Sources Sci. Technol.* **2014**, *23*, 065020.

(25) Uchida, G.; Nakajima, A.; Ito, T.; Takenaka, K.; Kawasaki, T.; Koga, K.; Shiratani, M.; Setsuhara, Y. Effects of Nonthermal Plasma Jet Irradiation on the Selective Production of H_2O_2 and NO_2^- in Liquid Water. *J. Appl. Phys.* **2016**, *120*, 203302.

(26) Rumbach, P.; Bartels, D. M.; Sankaran, R. M.; Go, D. B. The Solvation of Electrons by an Atmospheric-pressure Plasma. *Nat. Commun.* **2015**, *6*, 7248.

(27) Shirai, N.; Uchida, S.; Tochikubo, F.; Ishii, S. Self-organized Anode Pattern on Surface of Liquid or Metal Anode in Atmospheric DCGlow Discharges. *IEEE Trans. Plasma Sci.* **2011**, *39*, 2652−2653.

(28) Trelles, J. P. Pattern Formation and Self-organization in Plasmas Interacting with Surfaces. *J. Phys. D: Appl. Phys.* **2016**, *49*, 393002.

(29) Norberg, S. A.; Johnsen, E.; Kushner, M. J. Formation of Reactive Oxygen and Nitrogen Species by Repetitive Negatively Pulsed Helium Atmospheric Pressure Plasma Jets Propagating into Humid Air. *Plasma Sources Sci. Technol.* **2015**, *24*, 35026.

(30) Lin, L.; Lyu, Y.; Shneider, M. N.; Keidar, M. Average Electron Temperature Estimation of Streamer Discharge in Ambient Air. *Rev. Sci. Instrum.* **2018**, *89*, 113502.

(31) Keidar, M. Therapeutic Approaches Based on Plasmas and Nanoparticles. *J. Nanomedicine Res.* **2016**, *3*, 00052.

(32) Keidar, M.; Yan, D.; Beilis, I. I.; Trink, B.; Sherman, J. H. Plasmas for Treating Cancer: Opportunities for Adaptive and Self-Adaptive Approaches. *Trends Biotechnol.* **2018**, *36*, 586−593.

(33) Lyu, Y.; Lin, L.; Gjika, E.; Lee, T.; Keidar, M. Mathematical Modeling and Control for Cancer Treatment with Cold Atmospheric Plasma Jet. *J. Phys. D: Appl. Phys.* **2019**, *52*, 185202.

(34) Gjika, E.; Pal-Ghosh, S.; Tang, A.; Kirschner, M.; Tadvalkar, G.; Canady, J.; Stepp, M. A.; Keidar, M. Adaptation of Operational Parameters of Cold Atmospheric Plasma for in Vitro Treatment of Cancer Cells. *ACS Appl. Mater. Interfaces* **2018**, *10*, 9269−9279.

(35) Norberg, S. A.; Johnsen, E.; Kushner, M. J. Helium Atmospheric Pressure Plasma Jets Touching Dielectric and Metal Surfaces. *J. Appl. Phys.* **2015**, *118*, 013301.

(36) Cheng, X.; Sherman, J. H.; Murphy, W.; Ratovitski, E.; Canady, J.; Keidar, M. The Effect of Tuning Cold Plasma Composition on Glioblastoma Cell Viability. *PLoS One* **2014**, *9*, No. e98652.

(37) Siu, A.; Volotskova, O.; Cheng, X.; Khalsa, S. S.; Bian, K.; Murad, F.; Keidar, M.; Sherman, J. H. Differential Effects of Cold Atmospheric Plasma in the Treatment of Malignant Glioma. *PLoS One* **2015**, *10*, No. e0126313.

(38) Georgescu, N.; Lupu, A. R. Tumoral and Normal Cells Treatment with High-voltage Pulsed Cold Atmospheric Plasma Jets. *IEEE Trans. Plasma Sci.* **2010**, *38*, 1949−1955.

(39) Schmidt, J. W.; Moldover, M. R. Dielectric Permittivity of Eight Gases Measured with Cross Capacitors. *Int. J. Thermophys.* **2003**, *24*, 375−403.

(40) Zarnik, M. S.; Belavic, D. An Experimental and Numerical Study of the Humidity Effect on the Stability of a Capacitive Ceramic Pressure Sensor. *Radioengineering* **2012**, *21*, 201−206.

(41) Sakiyama, Y.; Graves, D. B.; Stoffels, E. Influence of Electrical Properties of Treated Surface on RF-Excited Plasma Needle at Atmospheric Pressure. *J. Phys. D: Appl. Phys.* **2008**, *41*, 095204.

(42) Shashurin, A.; Shneider, M. N.; Keidar, M. Measurements of Streamer Head Potential and Conductivity of Streamer Column in

Cold Nonequilibrium Atmospheric Plasmas. *Plasma Sources Sci. Technol.* **2012**, *21*, 034006.

(43) Shashurin, A.; Shneider, M. N.; Dogariu, A.; Miles, R. B.; Keidar, M. Temporary-resolved Measurement of Electron Density in Small Atmospheric Plasmas. *Appl. Phys. Lett.* **2010**, *96*, 171502.